

RESEARCH ARTICLE

10.1002/2015JA021610

Key Points:

- Solar energetic electrons map Mercury's magnetospheric topology
- Solar wind electrons likely produce polar rain at Mercury
- MeV electrons can be quasi-trapped in Mercury's magnetotail

Correspondence to:

D. J. Gershman,
danielj.gershman@nasa.gov

Citation:

Gershman, D. J., et al. (2015), MESSENGER observations of solar energetic electrons within Mercury's magnetosphere, *J. Geophys. Res. Space Physics*, 120, 8559–8571, doi:10.1002/2015JA021610.

Received 23 JUN 2015

Accepted 3 SEP 2015

Accepted article online 5 SEP 2015

Published online 24 OCT 2015

MESSENGER observations of solar energetic electrons within Mercury's magnetosphere

Daniel J. Gershman^{1,2}, Jim M. Raines², James A. Slavin², Thomas H. Zurbuchen², Brian J. Anderson³, Haje Korth³, George C. Ho³, Scott A. Boardson⁴, Timothy A. Cassidy⁵, Brian M. Walsh⁶, and Sean C. Solomon^{7,8}

¹Geospace Physics Laboratory, NASA Goddard Space Flight Center, Greenbelt, Maryland, USA, ²Department of Atmospheric, Oceanic and Space Sciences, University of Michigan, Ann Arbor, Michigan, USA, ³The Johns Hopkins University Applied Physics Laboratory, Laurel, Maryland, USA, ⁴Heliophysics Science Division, NASA Goddard Space Flight Center, Greenbelt, Maryland, USA, ⁵Laboratory for Atmospheric and Space Physics, University of Colorado Boulder, Boulder, Colorado, USA, ⁶Space Science Laboratory, University of California, Berkeley, California, USA, ⁷Lamont-Doherty Earth Observatory, Columbia University, Palisades, New York, USA, ⁸Department of Terrestrial Magnetism, Carnegie Institution of Washington, Washington, District of Columbia, USA

Abstract During solar energetic particle (SEP) events, the inner heliosphere is bathed in MeV electrons. Through magnetic reconnection, these relativistic electrons can enter the magnetosphere of Mercury, nearly instantaneously filling the regions of open field lines with precipitating particles. With energies sufficient to penetrate solid aluminum shielding more than 1 mm thick, these electrons were observable by a number of sensors on the Mercury Surface, Space ENvironment, GEOchemistry, and Ranging (MESSENGER) spacecraft. Because of its thin shielding, frequent sampling, and continuous temporal coverage, the Fast Imaging Plasma Spectrometer provided by far the most sensitive measurements of MeV electrons of all MESSENGER sensors. Sharp changes in energetic electron flux coincided with topological boundaries in the magnetosphere, including the magnetopause, polar cap, and central plasma sheet. Precipitating electrons with fluxes equal to ~40% of their corresponding upstream levels were measured over the entire polar cap, demonstrating that electron space weathering of Mercury's surface is not limited to the cusp region. We use these distinct precipitation signatures acquired over 33 orbits during 11 SEP events to map the full extent of Mercury's northern polar cap. We confirm a highly asymmetric polar cap, for which the dayside and nightside boundary latitudes range over ~50–70°N and ~30–60°N, respectively. These latitudinal ranges are consistent with average models of Mercury's magnetic field but exhibit a large variability indicative of active dayside and nightside magnetic reconnection processes. Finally, we observed enhanced electron fluxes within the central plasma sheet. Although these particles cannot form a stable ring current around the planet, their motion results in an apparent trapped electron population at low latitudes in the magnetotail.

1. Introduction

During maxima in solar activity, large quantities of energy and mass are frequently released from the Sun in the form of solar flares and coronal mass ejections (CMEs). Both the site of the initial flare at the surface of the Sun and the CME-driven shocks in the interplanetary medium serve as charged particle accelerators [Reames, 1995; Cliver and Cane, 2002]. Fluxes in excess of 10^3 particles cm^{-2} sr^{-1} s^{-1} MeV^{-1} of solar energetic particles (SEPs), both ions and electrons, are observed in situ by spacecraft in the heliosphere and can persist on timescales ranging from several hours to several days [Cane et al., 1988]. The most intense SEP events have been observed close to the Sun (within ~0.3–0.5 AU), first by the Helios spacecraft [Cane et al., 1990; Lario et al., 2006] and more recently by the Mercury Surface, Space ENvironment, GEOchemistry, and Ranging (MESSENGER) spacecraft [Solomon et al., 2001] while in orbit around Mercury [Lario et al., 2013]. Here we examine the interaction of MeV electrons from SEP events with Mercury's magnetosphere, an environment that hosts the most intense space weathering processes in the solar system.

Because they travel at a significant fraction of the speed of light, energetic electrons can be used to map magnetospheric topology. Electron distributions are typically subsonic in space plasmas [Pilipp et al., 1987], so that a substantial fraction of the distribution streams along the magnetic field in the opposite direction to that of the bulk plasma flow. In addition, in the nominal solar wind, there is a ~5% "strahl" of suprathermal

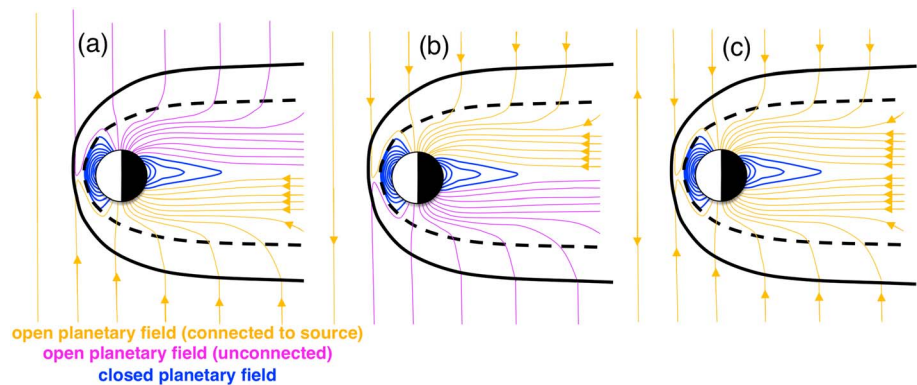


Figure 1. North-south cross sections of magnetic field topology in Mercury's magnetosphere. The interplanetary magnetic field maps to Mercury's polar cap via the magnetic lobes in the tail. Both ends of closed magnetic field lines (blue) are connected to the planet. Electrons in the solar wind from the suprathermal strahl or SEP events stream along the field lines; gold arrows indicate particle flow directions (rather than magnetic field directions). Antisunward streaming electrons flow into either the (a) southern or (b) northern hemisphere depending on the sector of the interplanetary magnetic field (e.g., outward or inward, respectively). (c) For bidirectional streaming or isotropic distributions, energetic electrons flow into both hemispheres.

(~ 100 eV) electrons that flows within $\sim 15^\circ$ of the magnetic field direction away from the Sun [Marsch, 2006]. Through magnetic reconnection at a planetary magnetopause, the solar wind field can become connected to that of the planet. The electron strahl is then free to stream backward along the magnetic field into the magnetosphere and toward the planet, independent of the bulk plasma flow. This kinetic-scale phenomenon is known as "polar rain" at Earth, where precipitation of ~ 100 eV electrons occurs over the entire polar cap [Winningham and Heikkila, 1974; Gussenhoven et al., 1984; Fairfield and Scudder, 1985; Baker et al., 1986]. At Earth, this lower-energy electron precipitation is rarely sufficient to generate auroral emissions [Zhang et al., 2007], so it is not typically observable with remote sensing techniques.

Because the electron strahl flow direction is almost always antisunward, electron precipitation may favor either the southern (Figure 1a) or northern (Figure 1b) hemisphere, depending on the sector (e.g., outward or inward) of the draped interplanetary magnetic field. For bidirectional streaming events, polar rain can occur over both the northern and southern hemispheres (Figure 1c) [Gosling et al., 1986]. Similar physics holds for more energetic electrons. Energetic electrons at the onset of SEP events are initially measured to be highly anisotropic, field-aligned populations, but quickly (within ~ 1 day) evolve to near isotropy, with MeV electrons flowing both sunward and antisunward in the frame of the planetary magnetosphere [Bieber et al., 1980; Kahler, 2007]. These reservoirs of MeV electrons fill both the northern and southern open-field regions at nearly the speed of light (Figure 1c). Energetic electrons can therefore be used as key signatures for the boundary of polar cap, which is important for the evaluation of both the magnetospheric open flux budget [Slavin et al., 2010; Milan and Slavin, 2011; Johnson et al., 2012] and space weathering of Mercury's surface [Madedy et al., 1998; Domingue et al., 2014]. This boundary has been mapped in an average sense from magnetic field and thermal plasma measurements [Korth et al., 2014]. However, Mercury's offset dipole field creates a "plasma void" in which closed-field particles are preferentially lost onto the southern hemisphere. This void is equatorward of the boundary between open and closed field lines, and the true nightside polar cap boundary has not yet been identified with in situ observations.

There are a number of physical quantities that describe the degree of adiabatic character (i.e., "adiabaticity") of particle motions in a magnetosphere. These parameters typically compare the size of a particle gyroradius to the local field line curvature [Speiser, 1965; Büchner and Zelenyi, 1989]. Parameters estimated for Mercury reveal that energetic particles should undergo substantial nonadiabatic motion, particularly in the neutral sheet in Mercury's magnetotail [Delcourt et al., 2003, 2005; Korth et al., 2012]. Trajectories of electrons in Mercury's magnetosphere have been estimated from test particle simulations [Ip, 1987; LeBlanc et al., 2003; Delcourt et al., 2005; Schriver et al., 2011a] and show substantial alteration of magnetic moments both in pitch angle and in energy during transits of electrons through the neutral sheet. Furthermore, it has been shown that Mercury's magnetosphere is so small that it cannot sustain an energetic particle ring current, although quasi-trapped populations that persist for tens of seconds may be possible given the right combinations

of injection locations and energies [Schriver *et al.*, 2011b; Walsh *et al.*, 2013]. Kinetic hybrid simulations reveal similar nonadiabatic behavior for ions [Trávníček *et al.*, 2009] but treat electrons as a neutralizing fluid such that electron nonadiabaticity is not dynamically considered. Finally, in addition to creating sharp gradients in the magnetic field, the magnetotail is home to plasma waves and instabilities. Magnetic turbulence at all observable scales ($\sim 10^{-3}$ – 10^1 Hz) has been seen to maximize in the low-latitude plasma sheet [Uritsky *et al.*, 2011; Boarden *et al.*, 2012]. Wave-particle interactions in this region may play a strong role in electron dynamics but are not easily evaluated with static-field test particle simulation techniques.

Bursts of locally generated ~ 30 – 300 keV electrons have been observed in Mercury's magnetosphere by both the Mariner 10 [Simpson *et al.*, 1974; Ogilvie *et al.*, 1977; Baker, 1986; Christon *et al.*, 1987] and the MESSENGER [Ho *et al.*, 2011a, 2011b] spacecraft. Bow shock processes and magnetic reconnection have been invoked as possible acceleration mechanisms of these electrons, but the temporal and spatial locations of these bursts [Ho *et al.*, 2012; Lawrence *et al.*, 2015] do not provide a clear correlation with known magnetospheric activity or invariant latitude that might diagnose the relevant energization processes. Understanding the behavior of electrons at all energies, in particular, those that are highly nonadiabatic, may elucidate the origin of accelerated planetary electrons.

Here we use data from the Fast Imaging Plasma Spectrometer (FIPS) [Andrews *et al.*, 2007] on MESSENGER to investigate the dynamics of electrons from SEP events in Mercury's magnetosphere. We demonstrate that FIPS, because of its thin aluminum shielding and $\sim 1.5\pi$ sr field of view, served as a highly sensitive detector of MeV electrons. Sharp gradients in measured electron flux provide a basis for identifying the boundaries of Mercury's polar cap and investigating electron dynamics in Mercury's magnetotail. These observations provide new insight into both magnetospheric dynamics and space weathering processes at Mercury.

2. Energetic Particle Detection With FIPS

The Energetic Particle and Plasma Spectrometer on the MESSENGER spacecraft consisted of two sensors, the Energetic Particle Spectrometer (EPS) and FIPS, intended to measure energetic and thermal plasma populations, respectively [Andrews *et al.*, 2007]. FIPS implemented an electrostatic system combined with a position-sensitive time-of-flight (TOF) telescope to measure the composition and dynamic properties of solar wind and magnetospheric ions in the energy range 10 eV/e to 13.7 keV/e. EPS had sets of solid-state detectors (SSDs) designed to measure ions and electrons with energies greater than 5 keV/nucleon and 35 keV, respectively.

Because of the limited shielding of the EPS sensor unit, MeV ions and electrons in SEP events had sufficient energies to generate measureable signals on all EPS SSDs [Ho *et al.*, 2011a]. Consequently, the relative contribution of each SEP species to the measured count rates cannot readily be determined. FIPS used micro-channel plates (MCPs) that were sensitive not only to low-energy ions and electrons but also to ultraviolet and X-ray photons and energetic particles [Wiza, 1979]. Solar energetic protons and electrons with energies greater than ~ 10 MeV and ~ 0.5 MeV, respectively, should have sufficient energies to penetrate both the ~ 0.5 mm thick aluminum TOF shell and high-voltage housing plates [Daly *et al.*, 1996]. Once inside the ~ 1 mm thick radiation shield, particles could either trigger the MCPs directly or, for electrons, generate bremsstrahlung X-rays through interactions with the sensor walls [Stassinopoulos and Raymond, 1988]. Particles also underwent angular scattering as they penetrated the material [Carron, 2007].

To estimate SEP penetration through the FIPS housing, we used the MULti-LAYered Shielding Simulation Software tool [Lei, *et al.*, 2002], which employs a one-dimensional Monte Carlo model of particle passage through matter. A solar energetic electron flux spectral shape of E^{-3} from Dröge [1995], where E is the electron energy, was imposed on a 1 mm thick layer of aluminum. Approximately $\sim 1\%$ of energetic electrons with energies in excess of ~ 1 MeV penetrated the FIPS shielding. Only $\sim 0.3\%$ of the incident electrons were converted into bremsstrahlung X-rays. Similarly, a $\sim E^{-4}$ spectral shape for protons was used following the "worst day" shock event at Earth from the Cosmic Ray Effects on Micro-Electronics Code [Tylka *et al.*, 1997]. We find $\sim 30\%$ transmission of energetic protons with energies in excess of ~ 10 MeV through the FIPS instrument housing.

Nominally, the FIPS field of view (FOV) was $\sim 1.4\pi$ sr with cutouts below 15° and above 75° from its boresight direction because of ion optic constraints. With spacecraft obstructions, this FOV was further reduced to $\sim 1.15\pi$ sr. To first order, we model the FIPS FOV of penetrating SEP particles as a hemisphere about its

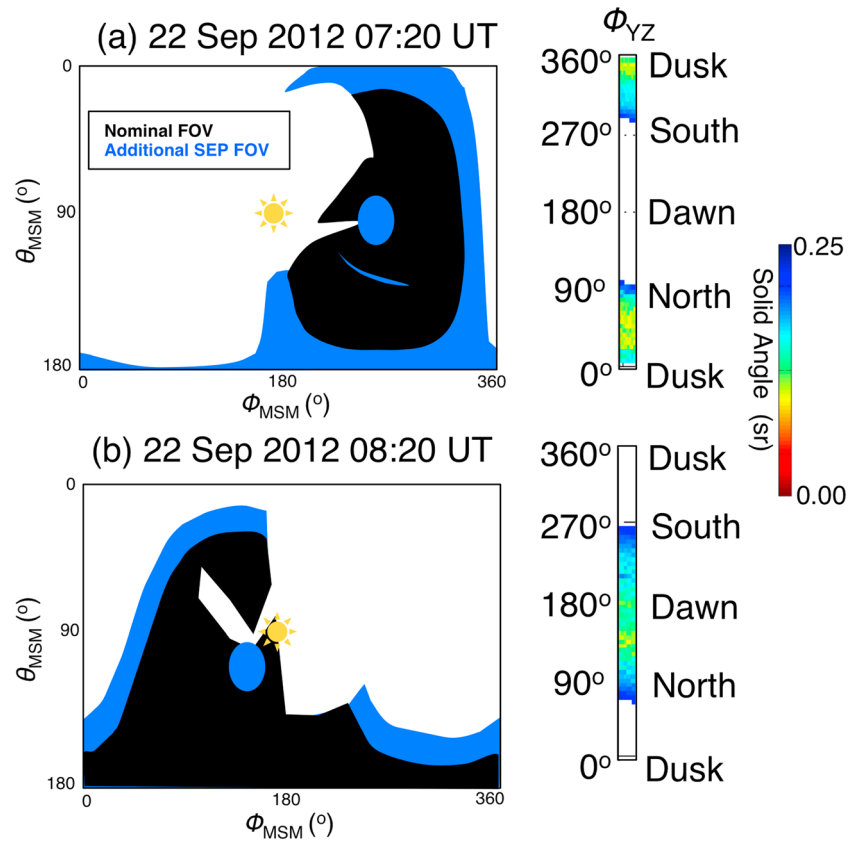


Figure 2. FIPS FOV for orientations of the MESSENGER spacecraft on (a) 22 September 2012, 07:20 UTC, and (b) 22 September 2012, 08:20 UTC. The FIPS FOV is shown in the MSM coordinates θ_{MSM} and ϕ_{MSM} , the polar and azimuthal angles, respectively. $(\theta_{\text{MSM}}, \phi_{\text{MSM}}) = (90^\circ, 180^\circ)$ corresponds to the solar direction. The nominal FIPS FOV is indicated in black and includes cutouts due to spacecraft obstructions and a $\sim 15^\circ$ circle centered around the FIPS boresight vector, which is confined to near the Y-Z plane. During SEP events, the additional blue FOV becomes visible because particles are not constrained by the FIPS electrostatic system. White areas are not sampled by FIPS in either case. On the right, the solid angle visible to FIPS during SEP events for two MESSENGER orientations has been projected onto the Y-Z plane (see the color bar on the far right). For the orientations in Figures 2a and 2b, FIPS pointed duskward and downward, respectively. The total visible solid angle was $\sim 1.5\pi$ sr. Similar visualizations have been described in more detail by Gershman *et al.* [2013, 2014a, 2014b].

boresight vector with only spacecraft obstructions, providing a field of view of $\sim 1.5\pi$ sr (Figure 2). The MESSENGER spacecraft was three-axis stabilized and had a protective sunshade that always pointed sunward. Consequently, spacecraft maneuvers were largely limited to rolls about the Sun-Mercury line. We use the Mercury solar magnetospheric (MSM) coordinate system in which the X-Y plane is offset ~ 484 km northward of the planetary center along Mercury's spin axis (along which the Z axis points northward), the X axis points sunward along the Sun-Mercury line, and the Y axis points duskward and completes the right-handed coordinate system [Anderson *et al.*, 2011]. As shown in Figure 2 for two example MESSENGER orientations, the FIPS boresight direction pointed out of the side of the spacecraft. For each example, the solid angle sampled by FIPS has been projected onto the Y-Z plane to enable a visualization of the FIPS SEP FOV as a function of time. Similar visualizations were used by Gershman *et al.* [2013, 2014a] to model the FIPS FOV of interstellar He^+ pickup ion distribution functions. Here directions not visible to FIPS are shown in white. For Figure 2a, the FIPS boresight vector was pointed toward dawn ($-Y$). With its wide FOV, FIPS could view particles traveling duskward, northward, and southward. For Figure 2b, the FIPS boresight vector pointed between dusk ($+Y$) and southward ($-Z$), measuring particles traveling dawnward and northward.

In the nominal mode of operation for FIPS as a time-of-flight mass spectrometer, secondary electrons liberated from a carbon foil by incident ions were directed onto a "start" MCP detector (MCP1), where they opened a ~ 660 ns timing window. The incident particle then traversed the distance of the FIPS TOF chamber

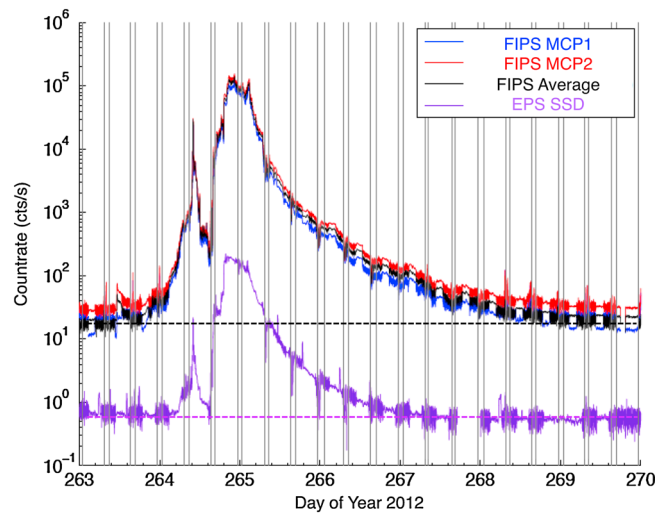


Figure 3. Energetic particle count rates for the FIPS MCPs (blue for MCP1, red for MCP2, and black for their average) and the EPS SSD 219 keV ion channel (purple) for a large SEP event at Mercury during the period 20–27 September 2012. The noise floors for each data set are shown as dashed lines. The onset of the event (counts measured above the noise floor) was observed on 23 and 24 September for FIPS and EPS, respectively. The event had two maxima simultaneously observed between 24 and 25 September by both sensors. The FIPS data provide an excellent proxy for energetic particle flux, with a factor of ~ 100 increased dynamic range over EPS for MeV electrons. Because both EPS and FIPS are sensitive to MeV protons and electrons, neither BG rate can be scaled directly to provide an absolute flux measurement. Shaded regions indicate time periods when MESSENGER was inside Mercury's magnetosphere.

channels. Energetic particles unfiltered by electrostatic analysis were present in all E/q channels. However, it was rare that thermal plasma simultaneously occupied the entire FIPS energy range. Therefore, to calculate background (BG) rates, we compare the average number of events in the lowest five ($E/q < 150$ eV/e) and highest five ($E/q > 10$ keV/e) channels. The lower of the two is taken as a reference count rate, N . We then take the average value over all E/q channels that have rates below the standard error associated with finite particle counting (i.e., $N + 1.96\sqrt{N}$) and normalize by the appropriate accumulation time. We first calculate BG rates for MCP1 and MCP2 individually and then again using their averaged E/q spectra.

Energetic electrons, bremsstrahlung X-rays, and energetic protons are expected to have detection efficiencies of $\sim 30\%$, 1% , and 1% on the FIPS MCPs, respectively [Wiza, 1979; Harres et al., 2008]. After scaling these efficiencies by their relative particle transmissions, we conclude that the background signals on the FIPS MCPs in SEP events were due to direct incidence of penetrating particles. Given an MCP area of ~ 10 cm² with a $\sim 0.75\pi$ sr effective FOV, cumulative fluxes of ~ 10 cm⁻² s⁻¹ of >1 MeV electrons and >10 MeV protons each correspond to a FIPS BG rate of ~ 1 count/s.

Consider an example SEP event from 18–26 September 2012. Energetic particle count rates from both EPS and FIPS for this time period are compared in Figure 3. The EPS data are taken from its SSD 219 keV ion channel, which provided the largest dynamic range in count rate, defined as the ratio of the maximum number of counts measured during the event to the EPS BG rate of $\sim 10^2$. The FIPS BG rate is in excellent agreement with the EPS data, but with a higher dynamic range of $\sim 10^4$. This increase in sensitivity provides visibility during the entire energetic particle event, not accessible previously. Indeed, the FIPS record nearly doubles the observed duration of the event relative to the EPS record, for which rates over the noise floor persisted for ~ 6 and ~ 3 days, respectively. Finally, there were apparent dips in electron fluxes from 21 to 23 September 2012 in both data sets that correspond to transits of Mercury's magnetosphere. These signatures are addressed in detail in section 3.

and generated a signal on an orthogonally mounted “stop” MCP detector (MCP2). If a stop signal was detected within that timing window, a TOF was calculated. This TOF, together with a known energy per charge, E/q , of the ion set by the electrostatic analyzer (ESA), enabled an estimate of the mass per charge. Because a penetrating particle was both unfiltered by the ESA and traveling at high speeds, it was unlikely to generate a valid start-stop pair. Coincidence measurements, therefore, provided a filter for energetic particles and served to increase the signal-to-noise ratio of space plasma instrumentation during SEP events [Gilbert et al., 2014]. However, because we use FIPS here as an energetic particle detector rather than a low-energy mass spectrometer, we consider the individual MCP1 and MCP2 detector rates and neglect the typically used start-stop coincidence rate.

A FIPS E/q scan occurred over a period of ~ 10 s or ~ 60 s in the sensor's burst and survey modes of operation, respectively, with corresponding integration times of either 0.05 or 0.95 s in 60 E/q

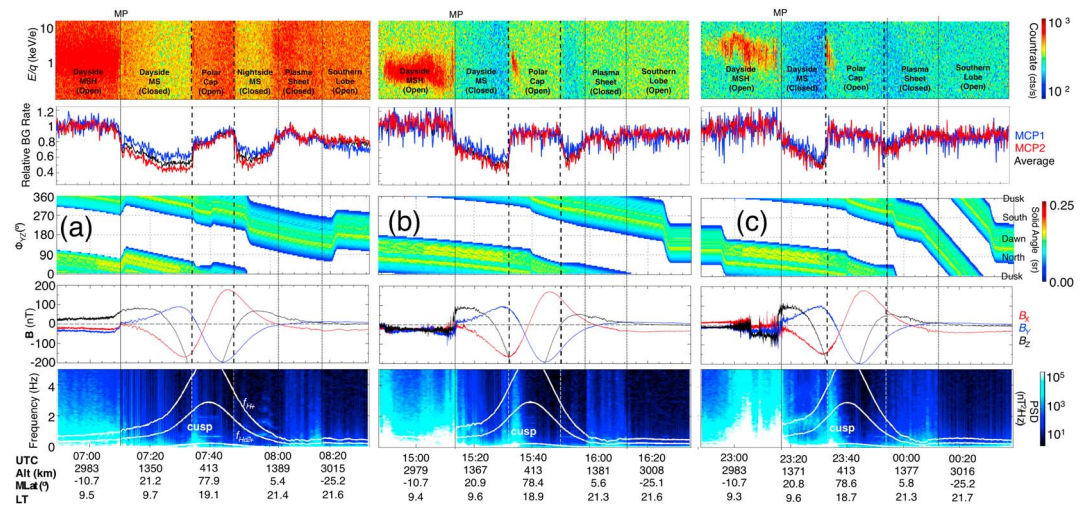


Figure 4. (a, b, c) Records of an SEP event during three successive MESSENGER orbits on 22 September 2012. (first row) Summed MCP1 and MCP2 detector rates. (second row) Individual MCP detector rates normalized by their respective near-MP values. (third row) The FIPS FOV projected onto the Y-Z plane (as described in Figure 2). (fourth row) The magnetic field vector. (fifth row) Power spectral density of magnetic fluctuations perpendicular to the mean field direction. The gyrofrequencies of H⁺ and He²⁺ are shown as solid white lines. For each orbit, the magnetopause, polar cap, and low-latitude plasma sheet regions are indicated as solid, dashed, and dotted lines, respectively. The FIPS BG rate dropped in the dayside closed-field region and increased both over the polar cap and in the low-latitude plasma sheet.

MESSENGER's Gamma-Ray and Neutron Spectrometer [Goldsten et al., 2007] has also been used to detect and characterize keV electron bursts at Mercury [Lawrence et al., 2015]. The Neutron Spectrometer and the anticoincidence shield on the Gamma-Ray Spectrometer also exhibited increased background signatures during SEP events but were configured to preferentially downlink high-time-resolution data when large variances (i.e., transient bursts) in electron fluxes were observed. Furthermore, data at the highest time resolution of ~10 ms were not acquired until 2013. Consequently, we do not consider data from these sensors in our analysis here. The full capabilities of these instruments with respect to electron observations have been described in detail by Lawrence et al. [2015]. FIPS was not sensitive to these lower-energy (i.e., < 1 MeV) electron bursts.

Energetic (>MeV) protons have gyroradii that are large (>1000 km) compared with the typical length scales of Mercury's magnetospheric system, so it is unlikely that they follow adiabatic charged-particle drift motion [Laurenza et al., 2011]. Electrons, however, even with near-relativistic energies, should have gyroradii on the order of 100 km, a small fraction of a Mercury radius (R_M) of ~2440 km. We therefore attribute changes in BG rates that match magnetospheric boundaries to changes in MeV electron flux. In locations where the energetic particle flux was highly directional, large changes in spacecraft orientation may have also resulted in changes in FIPS BG rates.

3. Results

Consider three successive magnetospheric transits during the 18–26 September 2012 SEP event shown in Figure 4. For these orbits, MESSENGER ascended from the dayside magnetosheath (MSH) across the magnetopause (MP) (solid line) over the northern polar cap (dashed lines), and then descended through the central plasma sheet (dotted lines) and southern magnetic lobe. From the top, the first row of Figures 4a–4c is FIPS E/q spectra summed from the MCP1 and MCP2 detectors. Calculated FIPS BG rates are shown for MCP1, MCP2, and their average in the second row of Figures 4a–4c. For each orbit, the BG rates are normalized relative to their near-MP values. Only after the signal from penetrating radiation has dropped down below ~500 counts/s do the signals from magnetospheric plasmas become visible. The calculated BG rates exclude the contribution from these thermal plasmas.

The third row of Figures 4a–4c visualizes the FIPS SEP FOV as a function of time. Transitions are due to changes in spacecraft attitude with time. The energetic particle fluxes do not appear to be a strong function of MESSENGER orientation, consistent with approximately isotropic upstream distributions. Instead, changes in flux are more coincident with magnetic boundaries as identified by the MESSENGER Magnetometer [Anderson *et al.*, 2007] (MAG) in the fourth and fifth rows of Figures 4a–4c. The spectrograms in the fifth row of Figures 4a–4c are calculated with a time-centered sliding window of 1 min duration, following Gershman *et al.* [2015]. MAG samples the ambient magnetic field with a maximum rate of 20 samples per second and a digitization resolution of ~ 0.05 nT [Anderson *et al.*, 2007].

Strong isotropic SEP fluxes were observed in the MSH as expected. On crossing the MP, however, there was a factor of ~ 2 reduction in measured BG rates. The relative changes in MCP1 and MCP2 across this boundary were not identical, an effect most pronounced in Figure 4a. BG rates rose sharply near the lower boundary of the magnetic cusp, as evidenced by a diamagnetic decrease in total magnetic field intensity, increased magnetic field inclination relative to the lobe field, and enhanced fluctuations in the magnetic field due to low-frequency waves observed in the magnetic spectrogram. The energetic electron fluxes here were likely highly anisotropic because of easier access of field-aligned entry particles to the surface. However, the attitude of the spacecraft was such that precipitating particles were well within the FIPS SEP FOV during these transits. A weak but measurable dependence on the MESSENGER orientation of the FIPS BG rate can be observed at 0740 LT when a BG rate increase from ~ 550 to ~ 700 counts/s corresponded to a northward turning of the spacecraft.

On the nightside, the BG rate dropped to its dayside closed-field levels with no corresponding signature in the magnetic field or spacecraft attitude. We interpret this drop as the nightside boundary of the polar cap where the planetary field was no longer directly connected to the solar wind. Because the MESSENGER transit of the polar cap was close to the planet, we use a simple dipole mapping of MESSENGER's location to invariant latitude, where the surface here is a sphere of radius R_M centered on the origin of the MSM coordinate system [Korth *et al.*, 2012]. The dayside (local time ~ 1000 h) and nightside (local time ~ 2100 h) latitudes for the examples in Figure 4 are (69° , 45°), (61° , 40°), and (64° , 35°), respectively.

The low nightside BG rate persisted until the spacecraft reached the central plasma sheet as identified by strong fluctuation power associated with diamagnetic depressions. The latitudinal range of these plasma sheet fluctuations can vary substantially, with the fluctuations in Figures 4a–4c poleward of $\sim 5^\circ$, $\sim 10^\circ$, and $\sim 60^\circ$ northern MSM latitudes, respectively. For the largest region of reduced fluxes in Figure 4a, transverse fluctuations were observed near the H^+ and He^{2+} gyrofrequencies, indicative of anisotropic thermal plasma. Once MESSENGER passed through this turbulent region, the BG rate remained high as the spacecraft passed through the southern magnetic lobe that was also directly connected to the interplanetary magnetic field.

We identified 33 orbits with 11 SEP events from March 2011 to October 2014 during which the boundaries of the polar cap were apparent on the basis of visible discontinuities in FIPS BG rates. The full list of these orbits and corresponding estimates of polar cap latitudes are given in Table A1 in Appendix A. These boundaries are shown as a function of local time in Figure 5 along with the average polar cap boundary estimated from the Alexeev *et al.* [2010] magnetic field model. Both the model and data show a strong day-night asymmetry, with dayside and nightside polar cap boundaries mapping to $\sim 50^\circ$ – 70° and $\sim 30^\circ$ – 60° , respectively. The data show increased variability over the average model, as expected for a dynamic magnetosphere. Shaded regions in Figure 5 illustrate the average regions where solar wind plasma had direct access to Mercury's surface. Direct ion and thermal electron precipitation is limited to the magnetic cusp regions [Zurbuchen *et al.*, 2011; Winslow *et al.*, 2014; Raines *et al.*, 2014]. However, energetic electrons are observed to precipitate over the entire area of the polar cap.

4. Discussion

Differences in the count rates of MCP1 and MCP2 are attributed to either an anisotropic response of each detector to incident particle flux or a difference in detection efficiency. In the closed-field region, the primary contribution of energetic particles to the FIPS BG rates should be MeV protons. The overall reduction of the FIPS BG rates in these regions implies that MeV electrons account for ~ 20 – 50% of the

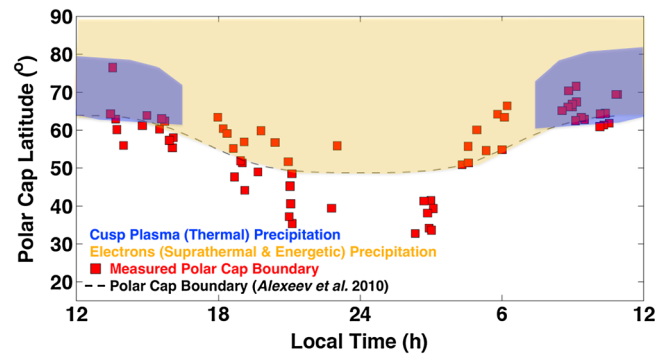


Figure 5. Map of Mercury's northern polar cap in invariant latitude as a function of local time. The average modeled boundary from Alexeev *et al.* [2010] is shown as a black dashed line. Regions where solar wind ions (blue) and electrons (gold), on average, have direct access to Mercury's surface under averaged conditions are shaded. Ions are confined to the cusp region, whereas energetic and polar rain electrons have access to the entire polar cap. Crossings of Mercury's polar cap identified by FIPS observations of energetic electrons are shown as red squares. These observations exhibit the strong day-night asymmetry predicted by the model but with increased variability.

the amount of magnetic flux that is simultaneously connected to both the solar wind and Mercury's planetary field. Any imbalance between dayside and nightside reconnection rates results in the expansion and contraction of the polar cap area, where the open field lines in the magnetic lobes converge at the planet [Burch, 1973; Milan, 2004]. From recent MESSENGER observations in the magnetic lobes, the typical range of estimated tail flux is 2.6 ± 0.6 MWb [Johnson *et al.*, 2012]. However, high rates of reconnection at the dayside magnetopause [Slavin *et al.*, 2009; DiBraccio *et al.*, 2013], >50% tail-loading events observed during the third MESSENGER flyby [Slavin *et al.*, 2010, 2012], and the extreme dayside magnetospheric erosion events observed during coronal mass ejections [Slavin *et al.*, 2014] suggest that large variations in the area of the polar cap must occur on occasion. As the solar wind magnetic field is convected antisunward, reconnected flux is transported from day to night and stretched out and loaded into Mercury's magnetotail. A pronounced day-night asymmetry in the polar cap latitude forms because of the small volume of the dayside magnetosphere. Our observations confirm this effect, though the polar cap size for these events is larger and more variable than those predicted by average models of Mercury's magnetosphere [Alexeev *et al.*, 2010; Korth *et al.*, 2014].

In the solar wind and magnetosheath, SEP fluxes were approximately isotropic in the frame of Mercury's magnetosphere, with particles traveling both sunward and antisunward. In these regions, with its $\sim 1.5\pi$ effective FOV, FIPS observed approximately $\sim 40\%$ of the upstream distribution. Over the polar cap and in the magnetospheric lobes, the fluxes were more anisotropic, but favorable orientation of MESSENGER resulted in FIPS observing nearly the entire distribution. For this reason, because the FIPS BG rates in the magnetosheath and over the polar cap were nearly identical, we conclude that $\sim 40\%$ of the upstream particles precipitate over the full area of Mercury's polar caps. The high energies of these particles may have resulted in increased electron-sputtering rates, where electrons have sufficient momentum to displace surface particles [LeBlanc *et al.*, 2003].

Although not directly observable with our measurement technique, as at Earth we expect that the precipitation pattern of energetic electrons from the solar wind should apply to suprathermal strahl electrons. These ~ 100 eV polar rain electrons lack sufficient energy for momentum-induced electronic sputtering. However, precipitating electrons at energies >10 eV can liberate both ion and neutral particles from Mercury's regolith through electron-stimulated desorption (ESD) [McLain *et al.*, 2011]. Desorption rates calculated from simulated electron precipitation suggest that ESD is an important source mechanism for exospheric production [Milillo *et al.*, 2005; Schriver *et al.*, 2011a], on par with ion sputtering. Solar wind precipitation is typically considered only in the cusp (Figure 5), where the

nominal BG signal, several times higher than might be expected from typical SEP events [Dröge, 1995; LeBlanc *et al.*, 2003]. However, a modest reduction in the MeV proton flux in the closed-field regions may account for this discrepancy. Finally, because the relative rates of MCP1 and MCP2 were similar in the upstream MSH (i.e., isotropic flux) and over the polar cap (i.e., anisotropic flux), we conclude that angular scattering of penetrating radiation obscured their initial incident directions so that each FIPS MCP acted as a near-omnidirectional sensor. Differences in MCP1 and MCP2 count rates are therefore attributed to differences in particle detection efficiencies.

Magnetic reconnection at the dayside magnetopause and at the near-Mercury neutral line (NMNL) controls

thermal plasmas have direct access to the surface [Schriver *et al.*, 2011a; Domingue *et al.*, 2014]. A kinetic description of electrons is needed to produce polar rain effects near Mercury, and such simulations do not exist as yet.

Our observations suggest that there may be a systematic underestimation of the total rate and spatial scale of ESD in current exospheric models of Mercury. For example, such a near-global source of space weathering may be responsible for the recent observed inhibition of thermal desorption of surface sodium into Mercury's exosphere [Cassidy *et al.*, 2014]. At Earth, ~ 100 eV polar rain electrons have fluxes of $\sim 10^6$ – 10^8 $\text{cm}^{-2} \text{s}^{-1}$ [Winningham and Heikkila, 1974]. From observations by the Helios spacecraft, the solar wind electron strahl population has been observed to be a constant fraction of the solar wind density between ~ 0.3 AU and 1 AU [Štverák *et al.*, 2009]. Therefore, we expect that Mercury's entire polar cap is regularly bombarded with $\sim 10^7$ – 10^9 $\text{cm}^{-2} \text{s}^{-1}$ fluxes of ~ 100 eV electrons, an order of magnitude less than the strong precipitation signatures predicted by Schriver *et al.* [2011a] but spread over a substantially larger area.

The lowest SEP electron fluxes are observed in the dayside closed-field region, consistent with minimal cross-field diffusive transport of electrons across the dayside MP. Magnetic reconnection on the dayside provides a pathway for energetic particles to permeate the magnetospheric lobes and precipitate onto Mercury's polar cap. Energetic electrons likely enter the closed field lines on the nightside via reconnection at the NMNL or diffusive transport/gradient drift entry [Hones *et al.*, 1972; Olson and Pfizter, 1985] across the equatorial duskside magnetopause in the low-latitude boundary layer (LLBL). For relativistic electrons, the equatorward $\mathbf{E} \times \mathbf{B}$ drift of ~ 50 km/s [Slavin *et al.*, 2012], where \mathbf{E} and \mathbf{B} are the electric and magnetic field vectors, respectively, is extremely small compared with their planetward speed, i.e., nearly the speed of light. Therefore, it is unlikely that a substantial fraction of lobe electrons can diffuse onto closed field lines before precipitating along open field lines. Increased electron fluxes on Mercury's nightside coincide directly with increased magnetic fluctuation power in the plasma sheet. Such a correlation suggests that on the timescale of a tail pass (~ 15 min), the variations in flux are due to spatial effects rather than temporal effects, which would show both increases and decreases in flux during a single transit.

Consider the adiabatic limit at Mercury. The gyroperiod, bounce period, and gradient curvature drift time across the magnetotail for a 1 MeV electron in a ~ 100 nT magnetic field are ~ 1 ms, ~ 10 ms, and ~ 2 s, respectively. For injection dominated by lobe reconnection, electrons would first enter the closed field lines that map to the highest invariant latitudes. The apex of these newly closed field lines will convect from the NMNL at $\sim (2-3) R_M$ downtail to the planet within ~ 3 s [Slavin *et al.*, 2012]. Because the particles' duskward drift speed is on the same order as this field line convection speed, it is unlikely that energetic electrons could populate field lines corresponding to the lowest invariant latitudes. Similarly, for particles entering in the duskside LLBL, test particle simulations show a bifurcation of electron drift paths near the terminator [Walsh *et al.*, 2013]. Only particles entering tailward of this bifurcation region ($L \sim 1.5 R_M$, where L is a parameter that describes the set of Mercury's magnetic field lines that cross the magnetic equator at a specified radius) can successfully drift across the tail at low latitudes. Because of MESSENGER's limited observational geometry, we cannot readily quantify the relative contribution of magnetic reconnection-based and LLBL-based entry mechanisms to the measured electron fluxes. However, neither process should produce energetic electron flux on closed field lines at low invariant latitudes in the magnetotail.

The MESSENGER trajectory through the magnetotail threaded the outermost closed field lines on both sides of the neutral sheet. For adiabatic and isotropic plasmas, the particle phase space density must be constant along a magnetic field line [Korth *et al.*, 2012, 2014]. However, reduced electron fluxes are observed in the near-planet ($< 1.5 R_M$) northern hemisphere but not in the far-tail ($> 2 R_M$) southern hemisphere, even though the magnetic field in each location maps to the same invariant latitude. The density of adiabatic plasma measured along a field line can exhibit a maximum at the equator if the distribution has a large ratio between the temperature perpendicular to the local magnetic field and the temperature parallel to the local field [Olsen *et al.*, 1994]. Therefore, increased energetic electron flux at low latitudes could result from adiabatic particle motion only if there is a preferential injection of electrons with pitch angles near 90° into the equatorial closed-field region.

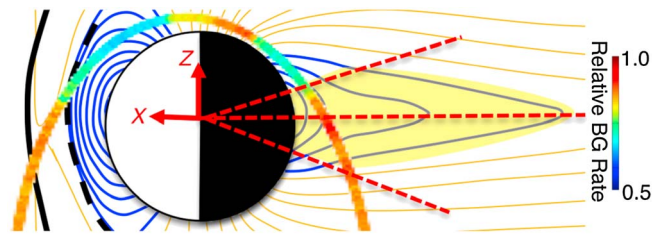


Figure 6. Relative FIPS BG rate from the 22 September 2012 event in Figure 4a along a projection of MESSENGER's orbit onto the MSM X-Z plane. The energetic electron flux dropped when MESSENGER crossed the magnetopause into the closed-field dayside region and when it crossed the nightside polar cap into the high-latitude closed-field region. Fluxes increased in the low-latitude plasma sheet coincident with turbulence fluctuations in the magnetic field (enclosed by red dashed lines). The lack of an observed reduction in flux in the closed-field region in the southern hemisphere may be due to the spacecraft trajectory. Although all magnetic latitudes were sampled, all invariant-MSM latitudes were not. Confinement of energetic electrons to only the low-MSM latitude for a given closed field line suggests highly nonadiabatic behavior.

However, near Mercury's neutral sheet it is unlikely that energetic electrons can satisfy this anisotropy requirement. Interaction with the turbulent fluctuations in the plasma sheet will result in pitch angle scattering, making it difficult to maintain a strong perpendicular anisotropy. Moreover, even in the absence of strong scattering, energetic electrons can execute meandering Speiser- or cucumber-type orbits about the neutral current sheet [Büchner and Zelenyi, 1989] due to their large gyroradii. The enhanced fluxes observed at low latitudes are most likely a result of MeV electrons spending disproportionate amounts of time near the neutral sheet, becoming quasi-trapped near the magnetic equator.

As evidenced in Figure 4a by the fluctuations near the H^+ and He^{2+} gyrofrequencies and low FIPS BG rates at high latitudes, closed-field thermal ions are present in locations where energetic electrons are not. An illustration of this trajectory is shown in Figure 6, where relative FIPS BG rates are painted onto a MESSENGER orbit that has been projected onto the X-Z plane. Analysis of wave activity near Mercury's plasma sheet [Boardsen et al., 2012, 2015] has revealed that the fluctuations are ordered by magnetic latitude rather than invariant latitude. Ray tracing of the ion-Bernstein wave mode along a single field line shows a transition from compressive to transverse fluctuation power within $\sim 10^\circ$ of the magnetic equator along the same field line [Boardsen et al., 2015]. Likewise, our observations are consistent with an energetic electron flux in the closed-field region that depends on MSM latitude (i.e., nonadiabatic trapping) rather than on invariant latitude (i.e., adiabatic bounce motion). Such dependence is specific to energetic electrons, whereas thermal ions are present at higher latitudes (Figure 4a). A number of the keV electron bursts reported by Ho et al. [2012] and Lawrence et al. [2015] occurred in similar geographic locations, suggesting that a fraction of their events could be attributed to quasi-trapped particles in the neutral sheet. However, the origin of these locally generated energetic particles at Mercury is still an open question.

5. Conclusions

We have used MESSENGER/FIPS background rates as a sensitive proxy for MeV electrons. Sharp changes in electron flux in these data correspond to magnetospheric boundaries such as the magnetopause, polar cap, and central plasma sheet. From observations acquired on 33 orbits during 11 SEP events at Mercury, we have mapped the extent of Mercury's northern polar cap as a function of local time, confirming the predicted day-night asymmetry. Unlike solar wind protons for which direct access to the surface is limited to the magnetic cusp region, suprathermal strahl and energetic solar electrons should have sufficient energies to precipitate over the full area of the polar cap, effects that are not currently captured in models of surface sputtering and its effect on neutral and charged particle production at Mercury. Finally, enhanced fluxes of energetic electrons in the nightside closed-field region are shown to correspond to strong magnetic turbulence in the plasma sheet. Such a confinement suggests that energetic electrons exhibit highly nonadiabatic behavior in Mercury's magnetotail.

Appendix A: Polar Cap Boundaries

A list of 33 polar cap boundaries inferred from FIPS observations of MeV electrons during 11 SEP events is provided in Table A1. The time in UTC, Mercury local time (LT) in hours, and invariant latitude are provided for each orbit.

Table A1. Mercury's Polar Cap Boundaries Inferred From FIPS Observations of MeV Electrons During SEP Events

Date	Dayside Boundaries			Nightside Boundaries		
	Time (hh:mm)	LT (h)	Invariant Latitude ($^{\circ}$)	Time (hh:mm)	LT (h)	Invariant Latitude ($^{\circ}$)
4 Aug 2011	08:56	6.2	66	09:07	16.1	58
7 Sep 2011	20:52	6.0	55	21:04	19.8	60
27 Jan 2012	22:53	15.7	62	23:03	5.8	64
28 Jan 2012	10:37	15.6	63	10:50	5.3	54
31 Jan 2012	09:22	15.0	64	09:33	4.9	60
1 Feb 2012	08:55	13.5	76	09:05	4.6	56
1 Feb 2012	20:40	14.8	61	20:55	4.3	51
5 Mar 2012	05:51	4.6	51	06:03	18.2	60
10 Mar 2012	01:53	16.1	55	02:11	3.0	33
10 Mar 2012	13:30	16.0	57	13:45	2.7	41
12 Mar 2012	00:20	15.5	60	00:37	2.3	33
27 May 2012	15:02	6.1	63	15:17	19.7	49
21 Sep 2012	15:32	10.5	62	15:47	21.1	49
21 Sep 2012	23:34	10.9	69	23:46	21.0	52
22 Sep 2012	07:34	10.8	69	07:48	21.0	45
22 Sep 2012	15:32	10.3	61	15:50	21.1	41
22 Sep 2012	23:33	10.4	64	23:54	21.1	35
23 Sep 2012	07:32	10.1	61	07:52	21.0	37
23 Sep 2012	23:33	10.1	64	23:45	20.4	57
28 Oct 2013	09:12	9.5	63	09:29	22.8	39
28 Oct 2013	17:17	9.3	63	17:29	23.0	56
8 Jan 2014	17:37	14.0	56	17:55	3.1	39
9 Jan 2014	01:35	13.7	63	01:53	2.9	34
9 Jan 2014	09:38	13.7	60	09:54	3.0	41
9 Jan 2014	17:37	13.4	64	17:53	2.8	38
1 Sep 2014	18:50	9.1	62	19:00	19.1	57
3 Sep 2014	02:59	9.1	67	03:10	19.0	51
3 Sep 2014	11:01	9.0	66	11:12	19.0	52
3 Sep 2014	19:03	9.0	67	19:18	19.1	44
4 Sep 2014	11:07	8.8	66	11:17	18.6	55
5 Sep 2014	03:12	9.1	72	03:20	18.4	59
5 Sep 2014	11:13	8.5	65	11:26	18.7	48
6 Sep 2014	03:18	8.8	70	03:25	18.0	63

Acknowledgments

We thank two anonymous reviewers for constructive comments on an earlier version of this paper. MESSENGER data are available from the Planetary Data System (http://ppi.pds.nasa.gov/MESS-E_V_H_SW-EPPS-3-FIPS-CDF-V1.0). The MESSENGER project is supported by the NASA Discovery Program under contracts NAS5-97271 to The Johns Hopkins University Applied Physics Laboratory and NASW-00002 to the Carnegie Institution of Washington. D.J.G. is supported by an appointment to the NASA Postdoctoral Program at Goddard Space Flight Center, administered by Oak Ridge Associated Universities.

Yuming Wang thanks two reviewers for their assistance in evaluating this paper.

References

- Alexeev, I. I., et al. (2010), Mercury's magnetospheric magnetic field after the first two MESSENGER flybys, *Icarus*, *209*, 23–39, doi:10.1016/j.icarus.2010.01.024.
- Anderson, B. J., M. H. Acuña, D. A. Lohr, J. Scheifele, A. Raval, H. Korth, and J. A. Slavin (2007), The Magnetometer instrument on MESSENGER, *Space Sci. Rev.*, *131*, 417–450.
- Anderson, B. J., C. L. Johnson, H. Korth, M. E. Purucker, R. M. Winslow, J. A. Slavin, S. C. Solomon, R. L. McNutt Jr., J. M. Raines, and T. H. Zurbuchen (2011), The global magnetic field of Mercury from MESSENGER orbital observations, *Science*, *333*, 1859–1862, doi:10.1126/science.1211001.
- Andrews, G. B., et al. (2007), The Energetic Particle and Plasma Spectrometer instrument on the MESSENGER spacecraft, *Space Sci. Rev.*, *131*, 523–556.
- Baker, D. N. (1986), Jovian electron populations in the magnetosphere of Mercury, *Geophys. Res. Lett.*, *13*, 789–792, doi:10.1029/GL013i008p00789.
- Baker, D. N., S. J. Bame, W. C. Feldman, J. T. Gosling, R. D. Zwickl, J. A. Slavin, and E. J. Smith (1986), Strong electron bidirectional anisotropies in the distant tail: ISEE 3 observations of polar rain, *J. Geophys. Res.*, *91*, 5637–5662, doi:10.1029/JA091iA05p05637.
- Bieber, J., J. Earl, G. Green, H. Kunow, R. Müller-Mellin, and G. Wibberenz (1980), Interplanetary pitch angle scattering and coronal transport of solar energetic particles: New information from Helios, *J. Geophys. Res.*, *85*, 2313–2323, doi:10.1029/JA085iA05p02313.
- Boardsen, S. A., J. A. Slavin, B. J. Anderson, H. Korth, D. Schriver, and S. C. Solomon (2012), Survey of coherent ~1 Hz waves in Mercury's inner magnetosphere from MESSENGER observations, *J. Geophys. Res.*, *117*, A00M05, doi:10.1029/2012JA017822.
- Boardsen, S. A., E.-H. Kim, J. M. Raines, J. A. Slavin, D. J. Gershman, B. J. Anderson, H. Korth, T. Sundberg, D. Schriver, and P. Travnicek (2015), Interpreting ~1 Hz magnetic compressional waves in Mercury's inner magnetosphere in terms of propagating ion-Bernstein waves, *J. Geophys. Res. Space Physics*, *120*, 4213–4228, doi:10.1002/2014JA020910.
- Büchner, J., and L. M. Zelenyi (1989), Regular and chaotic charged particle motion in magnetotaillike field reversals: 1. Basic theory of trapped motion, *J. Geophys. Res.*, *94*, 11,821–11,842, doi:10.1029/JA094iA09p11821.
- Burch, J. L. (1973), Rate of erosion of dayside magnetic flux based on a quantitative study of the dependence of polar cusp latitude on the interplanetary magnetic field, *Radio Sci.*, *8*, 955–961, doi:10.1029/RS008i011p00955.
- Cane, H. V., D. V. Reames, and T. T. von Rosenvinge (1988), The role of interplanetary shocks in the longitude distribution of solar energetic particles, *J. Geophys. Res.*, *93*, 9555–9567, doi:10.1029/JA093iA09p09555.

- Cane, H. V., T. T. von Roseninge, and R. E. McGuire (1990), Energetic particle observations at the Helios 1 spacecraft of shocks associated with coronal mass ejections, *J. Geophys. Res.*, *95*, 6575–6579, doi:10.1029/JA095iA05p06575.
- Carron, N. J. (2007), *An Introduction to the Passage of Energetic Particles Through Matter*, 384 pp., CRC Press, Francis & Taylor Group, Boca Raton, Fla.
- Cassidy, T. A., A. W. Merkel, M. H. Burger, M. Sarantos, R. M. Killen, W. E. McClintock, and R. J. Vervack Jr. (2014), Mercury's seasonal sodium exosphere: MESSENGER orbital observations, *Icarus*, *248*, 547–559, doi:10.1016/j.icarus.2014.10.037.
- Christon, S. P., J. Feynman, and J. A. Slavin (1987), Dynamic substorm injections: Similar magnetospheric phenomena at Earth and Mercury, in *Magnetotail Physics*, edited by A. T. Y. Lui, pp. 393–400, Johns Hopkins Univ. Press, Baltimore, Md.
- Cliver, E. W., and H. V. Cane (2002), The last word: Gradual and impulsive solar energetic particle events, *Eos Trans. AGU*, *83*, 61–68, doi:10.1029/2002EO000040.
- Daly, E. J., A. Hilgers, G. Drolshagen, and H. D. R. Evans (1996), Space environment analysis: Experience and trends, in *Proceedings of the ESA 1996 Symposium on Environment Modelling for Space-Based Applications*, ESA SP-392, edited by W. Burke and T.-D. Guyenne, pp. 15–22, Eur. Space Res. and Technol. Center, Noordwijk, Netherlands.
- Delcourt, D. C., S. Grimald, F. Leblanc, J.-J. Berthelier, A. Millilo, A. Mura, S. Orsini, and T. E. Moore (2003), A quantitative model of the planetary Na⁺ contribution to Mercury's magnetosphere, *Ann. Geophys.*, *21*, 1723–1736, doi:10.5194/angeo-21-1723-2003.
- Delcourt, D. C., K. Seki, N. Terada, and Y. Miyoshi (2005), Electron dynamics during substorm dipolarization in Mercury's magnetosphere, *Ann. Geophys.*, *23*, 3389–3398, doi:10.5194/angeo-23-3389-2005.
- DiBaccio, G. A., J. A. Slavin, S. A. Boardsen, B. J. Anderson, H. Korth, T. H. Zurbuchen, J. M. Raines, D. N. Baker, R. L. McNutt Jr., and S. C. Solomon (2013), MESSENGER observations of magnetopause structure and dynamics at Mercury, *J. Geophys. Res. Space Physics*, *118*, 997–1008, doi:10.1002/jgra.50123.
- Domingue, D. L., et al. (2014), Mercury's weather-beaten surface: Understanding Mercury in the context of lunar and asteroidal space weathering studies, *Space Sci. Rev.*, *181*, 121–124, doi:10.1007/s11214-014-0039-5.
- Dröge, W. (1995), Solar energetic electrons: I. Multiple spacecraft observations, in *24th International Cosmic Ray Conference*, vol. 4, edited by N. Lucci and E. Lamanna, pp. 187–190, International Union of Pure and Applied Physics, Rome, Italy.
- Fairfield, D. H., and J. D. Scudder (1985), Polar rain: Solar coronal electrons in the Earth's magnetosphere, *J. Geophys. Res.*, *90*, 4055–4068, doi:10.1029/JA090iA05p04055.
- Gershman, D. J., G. Gloeckler, J. A. Gilbert, J. M. Raines, L. A. Fisk, S. C. Solomon, E. C. Stone, and T. H. Zurbuchen (2013), Observations of interstellar helium pickup ions in the inner heliosphere, *J. Geophys. Res. Space Physics*, *118*, 1389–1402, doi:10.1002/jgra.50227.
- Gershman, D. J., L. A. Fisk, G. Gloeckler, J. M. Raines, J. A. Slavin, T. H. Zurbuchen, and S. C. Solomon (2014a), The velocity distribution of pickup He⁺ measured at 0.3 AU by MESSENGER, *Astrophys. J.*, *788*, 124, doi:10.1088/0004-637X/788/1/24.
- Gershman, D. J., J. A. Slavin, J. M. Raines, T. H. Zurbuchen, B. J. Anderson, H. Korth, D. N. Baker, and S. C. Solomon (2014b), Ion kinetic properties in Mercury's pre-midnight plasma sheet, *Geophys. Res. Lett.*, *41*, 5740–5747, doi:10.1002/2014GL060468.
- Gershman, D. J., J. M. Raines, J. A. Slavin, T. H. Zurbuchen, T. Sundberg, S. A. Boardsen, B. J. Anderson, H. Korth, and S. C. Solomon (2015), MESSENGER observations of multiscale Kelvin-Helmholtz vortices at Mercury, *J. Geophys. Res. Space Physics*, *120*, 4354–4368, doi:10.1002/2014JA020903.
- Gilbert, J. A., D. J. Gershman, G. Gloeckler, R. A. Lundgren, T. H. Zurbuchen, T. M. Orlando, J. McLain, and R. von Steiger (2014), Characterization of background sources in space-based time-of-flight mass spectrometers, *Rev. Sci. Instrum.*, *85*, 091301, doi:10.1063/1.4894694.
- Goldsten, J. O., et al. (2007), The MESSENGER Gamma-Ray and Neutron Spectrometer, *Space Sci. Rev.*, *131*, 339–391, doi:10.1007/s11214-007-9262-7.
- Gosling, J. T., D. N. Baker, S. J. Bame, and R. D. Zwickl (1986), Bidirectional solar wind electron heat flux and hemispherically symmetric polar rain, *J. Geophys. Res.*, *91*, 11,352–11,358, doi:10.1029/JA091iA10p11352.
- Gusenhoven, M. S., D. A. Hardy, N. Heinemann, and R. K. Burkhardt (1984), Morphology of the polar rain, *J. Geophys. Res.*, *89*, 9785–9800, doi:10.1029/JA089iA11p09785.
- Harres, K., et al. (2008), Development and calibration of a Thomson parabola with microchannel plate for the detection of laser-accelerated MeV ions, *Rev. Sci. Instrum.*, *79*, 093306.
- Ho, G. C., R. D. Starr, R. E. Gold, S. M. Krimigis, J. A. Slavin, D. N. Baker, B. J. Anderson, R. L. McNutt Jr., L. R. Nittler, and S. C. Solomon (2011a), Observations of suprathermal electrons in Mercury's magnetosphere during the three MESSENGER flybys, *Planet. Space Sci.*, *59*, 2016–2025, doi:10.1016/j.pss.2011.01.011.
- Ho, G. C., et al. (2011b), MESSENGER observations of transient bursts of energetic electrons in Mercury's magnetosphere, *Science*, *333*, 1866–1868, doi:10.1126/science.1211001.
- Ho, G. C., S. M. Krimigis, R. E. Gold, D. N. Baker, B. J. Anderson, H. Korth, J. A. Slavin, R. L. McNutt Jr., R. M. Winslow, and S. C. Solomon (2012), Spatial distribution and spectral characteristics of energetic electrons in Mercury's magnetosphere, *J. Geophys. Res.*, *117*, A00M04, doi:10.1029/2012JA017983.
- Hones, E. W., Jr., J. R. Asbridge, S. J. Bame, M. D. Montgomery, S. Singer, and S.-I. Akasofu (1972), Measurements of magnetotail plasma flow made with Vela 4B, *J. Geophys. Res.*, *77*, 5503–5522, doi:10.1029/JA077i028p05503.
- Ip, W.-H. (1987), Dynamics of electrons and heavy ions in Mercury's magnetosphere, *Icarus*, *71*, 441–447.
- Johnson, C. L., et al. (2012), MESSENGER observations of Mercury's magnetic field structure, *J. Geophys. Res.*, *117*, E00L14, doi:10.1029/2012JE004217.
- Kahler, S. W. (2007), Solar sources of heliospheric energetic electron events—Shocks or flares?, *Space Sci. Rev.*, *129*, 359–390.
- Korth, H., B. J. Anderson, C. L. Johnson, R. M. Winslow, J. A. Slavin, M. E. Purucker, S. C. Solomon, and R. L. McNutt Jr. (2012), Characteristics of the plasma distribution in Mercury's equatorial magnetosphere derived from MESSENGER Magnetometer observations, *J. Geophys. Res.*, *117*, A00M07, doi:10.1029/2012JA018052.
- Korth, H., B. J. Anderson, D. J. Gershman, J. M. Raines, J. A. Slavin, T. H. Zurbuchen, S. C. Solomon, and R. L. McNutt Jr. (2014), Plasma distribution in Mercury's magnetosphere derived from MESSENGER Magnetometer and Fast Imaging Plasma Spectrometer observations, *J. Geophys. Res. Space Physics*, *119*, 2917–2932, doi:10.1002/2013JA019567.
- Lario, D., M.-B. Kallenrode, R. B. Decker, E. C. Roelof, S. M. Krimigis, A. Aran, and B. Sanahuja (2006), Radial and longitudinal dependence of solar 4–13 MeV and 27–37 MeV proton peak intensities and fluences: Helios and IMP 8 observations, *Astrophys. J.*, *653*, 1531–1544.
- Lario, D., G. C. Ho, E. C. Roelof, B. J. Anderson, and H. Korth (2013), Intense solar near-relativistic electron events at 0.3 AU, *J. Geophys. Res. Space Physics*, *118*, 63–73, doi:10.1002/jgra.50106.
- Laurenza, M., M. Storini, R. Vainio, and L. Desorgher (2011), Cutoff rigidities for Mercury-orbiting spacecraft, in *Proceedings of the 32nd International Cosmic Ray Conference*, 11, 436–438, Beijing, China, doi:10.7529/ICRC2011/V11/0230.
- Lawrence, D. J., et al. (2015), Comprehensive survey of energetic electron events in Mercury's magnetosphere with data from the MESSENGER Gamma-Ray and Neutron Spectrometer, *J. Geophys. Res. Space Physics*, *120*, 2851–2876, doi:10.1002/2014JA020792.

- Leblanc, F., J. G. Luhmann, R. E. Johnson, and M. Liu (2003), Solar energetic particle event at Mercury, *Planet. Space Sci.*, *51*, 339–352, doi:10.1016/S0032-0633(02)00207-6.
- Lei, F., P. R. Truscott, C. S. Dyer, B. Quaghebeur, D. Heynderickx, P. Nieminen, H. Evans, and E. Daly (2002), MULASSIS: A Geant4-based multilayered shielding simulation tool, *IEEE Trans. Nucl. Sci.*, *49*, 2788–2793, doi:10.1109/TNS.2002.805351.
- Madey, T. E., B. V. Yakshinskiy, V. N. Ageev, and R. E. Johnson (1998), Desorption of alkali atoms and ions from oxide surfaces: Relevance to origins of Na and K in atmospheres of Mercury and the Moon, *J. Geophys. Res.*, *103*, 5873–5887, doi:10.1029/98JE00230.
- Marsch, E. (2006), Kinetic physics of the solar corona and solar wind, *Living Rev. Sol. Phys.*, *3*, 1–100.
- McLain, J. L., A. L. Sprague, G. A. Grieves, D. Schriver, P. Travnickek, and T. M. Orlando (2011), Electron-stimulated desorption of silicates: A potential source for ions in Mercury's space environment, *J. Geophys. Res.*, *116*, E03007, doi:10.1029/2010JE003714.
- Milan, S. E. (2004), A simple model of the flux content of the distant magnetotail, *J. Geophys. Res.*, *109*, A07210, doi:10.1029/2004JA010397.
- Milan, S. E., and J. A. Slavin (2011), An assessment of the length and variability of Mercury's magnetotail, *Planet. Space Sci.*, *59*, 2058–2065.
- Milillo, A., et al. (2005), Surface-exosphere-magnetosphere system of Mercury, *Space Sci. Rev.*, *117*, 397–444.
- Ogilvie, K. W., J. D. Scudder, V. M. Vasyliunas, R. E. Hartle, and G. L. Siscoe (1977), Observations at the planet Mercury by the plasma electron experiment: Mariner 10, *J. Geophys. Res.*, *82*, 1807–1824, doi:10.1029/JA082i013p01807.
- Olsen, R. C., L. J. Scott, and S. A. Boardsen (1994), Comparison between Liouville's theorem and observed latitudinal distributions of trapped ions in the plasmopause region, *J. Geophys. Res.*, *99*, 2191–2203, doi:10.1029/93JA02776.
- Olson, W. P., and K. A. Pfitzer (1985), Magnetospheric responses to the gradient drift entry of solar wind plasma, *J. Geophys. Res.*, *90*, 10,823–10,833, doi:10.1029/JA090iA11p10823.
- Pilipp, W. G., H. Miggenrieder, M. D. Montgomery, K.-H. Mühlhäuser, H. Rosenbauer, and R. Schwenn (1987), Characteristics of electron velocity distribution functions in the solar wind derived from the Helios Plasma Experiment, *J. Geophys. Res.*, *92*, 1075–1092, doi:10.1029/JA092iA02p01075.
- Raines, J. M., D. J. Gershman, J. A. Slavin, T. H. Zurbuchen, H. Korth, B. J. Anderson, and S. C. Solomon (2014), Structure and dynamics of Mercury's magnetospheric cusp: MESSENGER measurements of protons and planetary ions, *J. Geophys. Res. Space Physics*, *119*, 6587–6602, doi:10.1002/2014JA020120.
- Reames, D. V. (1995), Solar energetic particles: A paradigm shift, *Rev. Geophys.*, *33*, 585–589, doi:10.1029/95RG00188.
- Schrifer, D., et al. (2011a), Quasi-trapped ion and electron populations at Mercury, *Geophys. Res. Lett.*, *38*, L23103, doi:10.1029/2011GL049629.
- Schrifer, D., et al. (2011b), Electron transport and precipitation at Mercury during the MESSENGER flybys: Implications for electron-stimulated desorption, *Planet. Space Sci.*, *59*, 2026–2036, doi:10.1016/j.pss.2011.03.008.
- Simpson, J. A., J. H. Eraker, J. E. Lamport, and P. H. Walpole (1974), Electrons and protons accelerated in Mercury's magnetic field, *Science*, *185*, 160–166, doi:10.1126/science.185.4146.160.
- Slavin, J. A., et al. (2009), MESSENGER observations of magnetic reconnection in Mercury's magnetosphere, *Science*, *324*, 606–610, doi:10.1126/science.1172011.
- Slavin, J. A., et al. (2010), MESSENGER observations of extreme loading and unloading of Mercury's magnetic tail, *Science*, *329*, 665–668, doi:10.1126/science.1188067.
- Slavin, J. A., et al. (2012), MESSENGER and Mariner 10 flyby observations of magnetotail structure and dynamics at Mercury, *J. Geophys. Res.*, *117*, A01215, doi:10.1029/2011JA016900.
- Slavin, J. A., et al. (2014), MESSENGER observations of Mercury's dayside magnetosphere under extreme solar wind conditions, *J. Geophys. Res. Space Physics*, *119*, 8087–8116, doi:10.1002/2014JA020319.
- Solomon, S. C., et al. (2001), The MESSENGER mission to Mercury: Scientific objectives and implementation, *Planet. Space Sci.*, *49*, 1445–1465, doi:10.1016/S0032-0633(01)00085-X.
- Speiser, T. W. (1965), Particle trajectories in model current sheets: 1. Analytical solutions, *J. Geophys. Res.*, *70*, 4219–4226, doi:10.1029/JZ070i017p04219.
- Stassinopoulos, E. G., and J. P. Raymond (1988), The space radiation environment for electronics, *Proc. IEEE*, *76*, 1423–1442.
- Štverák, Š., M. Maksimovic, P. M. Trávníček, E. Marsch, A. N. Fazakerley, and E. E. Scime (2009), Radial evolution of nonthermal electron populations in the low-latitude solar wind: Helios, Cluster, and Ulysses observations, *J. Geophys. Res.*, *114*, A05104, doi:10.1029/2008JA013883.
- Trávníček, P. M., P. Hellinger, D. Schriver, D. Herčík, J. A. Slavin, and B. J. Anderson (2009), Kinetic instabilities in Mercury's magnetosphere: Three-dimensional simulation results, *Geophys. Res. Lett.*, *36*, L07104, doi:10.1029/2008GL036630.
- Tylka, A. J., J. H. Adams, P. R. Boberg, B. Brownstein, W. F. Dietrich, E. O. Flückiger, E. L. Petersen, M. A. Shea, D. F. Smart, and E. C. Smith (1997), CREME96: A revision of the cosmic ray effects on micro-electronics code, *IEEE Trans. Nucl. Sci.*, *44*, 2150–2160.
- Uritsky, V. M., J. A. Slavin, G. V. Khazanov, E. F. Donovan, S. A. Boardsen, B. J. Anderson, and H. Korth (2011), Kinetic-scale magnetic turbulence and finite Larmor radius effects at Mercury, *J. Geophys. Res.*, *116*, A09236, doi:10.1029/2011JA016744.
- Walsh, B. M., A. S. Ryou, D. G. Sibeck, and I. I. Alexeev (2013), Energetic particle dynamics in Mercury's magnetosphere, *J. Geophys. Res. Space Physics*, *118*, 1992–1999, doi:10.1002/jgra.50266.
- Winningham, J. D., and W. J. Heikkilä (1974), Polar cap auroral electron fluxes observed with Isis 1, *J. Geophys. Res.*, *79*, 949–957, doi:10.1029/JA079i007p00949.
- Winslow, R. M., et al. (2014), Mercury's surface magnetic field determined from proton-reflection magnetometry, *Geophys. Res. Lett.*, *41*, 4463–4470, doi:10.1002/2014GL060258.
- Wiza, J. L. (1979), Microchannel plate detectors, *Nucl. Instrum. Methods*, *162*, 587–601.
- Zhang, Y., L. J. Paxton, and A. T. Y. Lui (2007), Polar rain aurora, *Geophys. Res. Lett.*, *34*, L20114, doi:10.1029/2007GL031602.
- Zurbuchen, T. H., et al. (2011), MESSENGER observations of the spatial distribution of planetary ions near Mercury, *Science*, *333*, 1862–1865, doi:10.1126/science.1211302.